Smart Structures and Systems, *Vol. 30, No. 1 (2022) 63-74*
https://doi.org/10.12989/sss.2022.30.1.063

Characterizing the strain transfer on the sensing cable-soil interface based on triaxial testing

Guan-Zhong Wu [1], Dan Zhang*[1,2], Tai-Song Shan [1], Bin Shi [1], Yuan-Jiang Fang [1] and Kang Ren [1]

[1] *School of Earth Sciences and Engineering, Nanjing University, Nanjing, Jiangsu 210093, China*
[2] *Key Laboratory of Earth Fissures Geological Disaster of Ministry of Land and Resources, Geological Survey of Jiangsu Province, Nanjing 210018, China*

(*Received August 23, 2021, Revised December 1, 2021, Accepted April 17, 2022*)

Abstract. The deformation coordination between a rock/soil mass and an optical sensing cable is an important issue for accurate deformation monitoring. A stress-controlled triaxial apparatus was retrofitted by introducing an optical fiber into the soil specimen. High spatial resolution optical frequency domain reflectometry (OFDR) was used for monitoring the strain distribution along the axial direction of the specimen. The results were compared with those measured by a displacement meter. The strain measured by the optical sensing cable has a good linear relationship with the strain calculated by the displacement meter for different confining pressures, which indicates that distributed optical fiber sensing technology is feasible for soil deformation monitoring. The performance of deformation coordination between the sensing cable and the soil during unloading is higher than that during loading based on the strain transfer coefficients. Three hypothetical strain distributions of the triaxial specimen are proposed, based on which theoretical models of the strain transfer coefficients are established. It appears that the parabolic distribution of specimen strain should be more reasonable by comparison. Nevertheless, the strain transfer coefficients obtained by the theoretical models are higher than the measured coefficients. On this basis, a strain transfer model considering slippage at the interface of the sensing cable and the soil is discussed.

Keywords: cable-soil interface; deformation coordination; distributed optical fiber sensing (DOFS); strain transfer; triaxial testing

1. Introduction

Land subsidence is one of the common geological disasters in coastal cities in eastern China. There are many reasons for this disaster, such as changes in groundwater level, additional loads caused by engineering construction, geotectonic movements, and the compression of unconsolidated newly deposited strata. Accurate and effective monitoring is an important means to study the mechanism, early warning and prevention of ground subsidence (Hu *et al*. 2004, Li *et al*. 2006a, Morton and Bernier 2010, O'Leary and Gottardi 2020, Wang *et al*. 2009).

The common monitoring technologies include Global Positioning System (GPS), Interferometric Synthetic Aperture Radar (InSAR), precision levelling, layerwise mark and bedrock mark (Gutiérrez *et al*. 2011, Yao and Mu 2008, Zhang *et al*. 2019), etc. However, these traditional monitoring techniques have some limitations in obtaining the deep continuous deformation of the entire stratum, which is important for the research and prevention of ground subsidence.

Due to the advantages of distributed, long-distance, anti-electromagnetic interference and high reliability, distributed optical fiber sensors (DOFSs) have been greatly developed and applied in geological and geotechnical fields (Feng *et al*. 2015, Habel and Krebber 2011, Leung *et al*. 2015, Tennyson *et al*. 2001). The deformation coordination between the optical fiber and the geological body is a key issue for deformation measurement (Al-Tarawneh *et al*. 2018, Ansari and Yuan 1998, Ansari 2007, Claus *et al*. 1989, Kesavan *et al*. 2005, Nanni *et al*. 1991, Zhang *et al*. 2017). Therefore, studies have been carried out to explore the interface characteristics between the optical fiber and the measured matrix, including the effects of the coating jacket and other buffers of the optical cables. (Billon *et al*. 2015, Iten 2011, Wan *et al*. 2008) A number of interface model theories are proposed (Wang and Zhou 2014). However, there are two problems in these studies: (1) The strain of the optical cable is the result of the soil deformation (Glisic and Yao 2012, Klar *et al*. 2014). However, the deformation coordination was explored by applying tension on the optical cable instead of on the soil, which makes the test results less representative and convincing. (2) There is no relationship between the real deformation of the soil and the deformation measured by the optical fiber.

In this paper, the deformation coordination between the sensing cable and soil is studied based on the triaxial test. An optical frequency domain reflectometer (OFDR) was used to monitor the deformation of the soil in the triaxial tests. The deformation relationship between the optical

*Corresponding author, Ph.D., Professor,
E-mail: zhangdan@nju.edu.cn

ISSN: 1738-1584 (Print), 1738-1991 (Online)

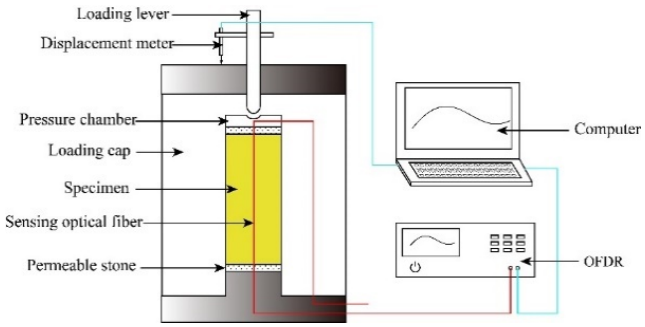

Fig. 1 Schematic illustration of the testing apparatus

cable and the soil is studied, and the theoretical models of the deformation relationship are established. This paper provides a reference and basis for the application of distributed optical fiber sensors for land subsidence monitoring.

2. Design of the experiments

2.1 Instruments

To study the deformation coordination between the sensing cable and the soil when the soil is compressed, a stress-controlled triaxial compression instrument was modified by introducing a 2 mm diameter sensing cable in the center of the triaxial sample, as shown in Fig. 1. The pressure chamber used in the test is a hollow cylinder made of plexiglass with a height of 22 cm and a diameter of 15 cm. O-rings are used to strengthen the connection between the pressure chamber and the base to ensure the impermeability of the pressure chamber. During the test, the pressure chamber is filled with water, and uniform confining pressure is applied to the sample through the air compressor.

The overall deformation of the sample is measured with a displacement meter with an accuracy of 0.01 mm. The internal deformation of the sample is measured by an OSI-S OFDR, which is made by ETSC (Hong Kong) Technologies Limited. The maximum measuring distance of the instrument is 100 m, the spatial resolution can reach 1 mm, and the sensing accuracy is 1 $\mu\varepsilon$. Compared with the optical fiber sensing technology of BOTDR and BOTDA, the instrument has superhigh strain measurement accuracy and spatial resolution, which is very suitable for the fine measurement of small-scale laboratory tests.

2.2 Materials and test specimens

The optical cable embedded in the soil is a 2 mm diameter single-mode optical cable that has been widely used in engineering monitoring. The main parameters of the optical cable are shown in Table 1. The triaxial specimen was made of silty clay. The basic properties of the soil are summarized in Table 2.

In preparation of the specimens, the optical fiber was first introduced from the bottom of the tray and pre-stretched to avoid bending. Then, the prepared silty clay (moisture content: 16%) was filled into a split tube with a bottom area of 30 mm^2 by three rounds of compaction. The density of the triaxial specimen is 1.725 g/cm^3. The specimen was coated with a rubber membrane. The optical cable was led out from the side of the top cap and finally was threaded out from the pedestal. After that, the confining pressure is applied on the specimen.

Table 1 Main parameters of the optical cable

Diameter /mm	Maximum breaking force/N	Elastic modulus/GPa	Strain range /με
2	220	0.37	-10000~+20000

2.3 Test procedure

The axial strain of the optical fiber and the vertical deformation of the sample are monitored simultaneously.

The confining pressures applied in this test are 200, 300, and 400 kPa. After the volume changes of the specimen were stabilized, the axial pressure was applied to the specimen step by step through the loading bar under the consolidated drainage condition. The maximum axial stress applied should not exceed 50% of the confining pressure, and the load increment of each step was 25 kPa. For example, the sequence of axial stress applied at a confining pressure of 300 kPa is 0, 25, 50, 75, 100, 125, 150, 125, 100, 75, 50, 25, and 0 kPa. The tests under three confining pressures were conducted on the same sample. Therefore, the soil sample and the sensing cable will produce irrecoverable strain after each loading and unloading cycle. It is necessary to clear the irrecoverable strain before conducting a new cycle.

3. Test results

3.1 Strain distribution of the optical sensing cable

The axial strain distribution of the optical cable during the loading and unloading process under different confining pressures was measured by OFDR. The test results are shown in Figs. 2-4. The cable strain is proportional to the axial stress. The strain distribution is nonuniform and approximatively symmetrical along the axial direction of the specimen. The strain at both ends of the specimen is smaller than that in the middle of the specimen. The cable strain under the condition of unloading is higher than that under the condition of loading at the same axial pressure mainly because of the plastic deformation of the soil, which results in residual compressive strain. For example, the maximum cable strain under 75 kPa axial pressure is 446 $\mu\varepsilon$ in the unloading process, as shown in Fig. 2(b), while that

Table 2 Basic properties of the test soil

Specific gravity G_s	Liquid limit w_L/%	Plastic limit I_p/%	Optimum moisture content w_{opt}/%	Maximum dry density /g/cm^3
2. 73	34.5	17.6	16.0	1.7

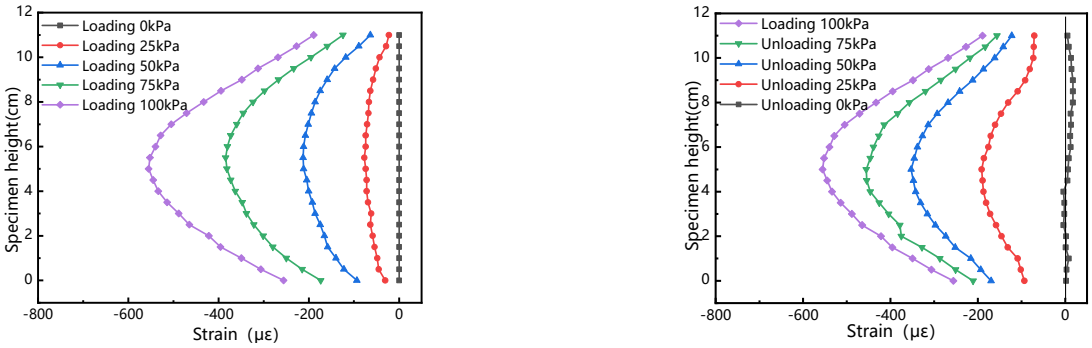

(a) Loading process (b) Unloading process

Fig. 2 Strain distribution of optical fiber under 200 kPa confining pressure

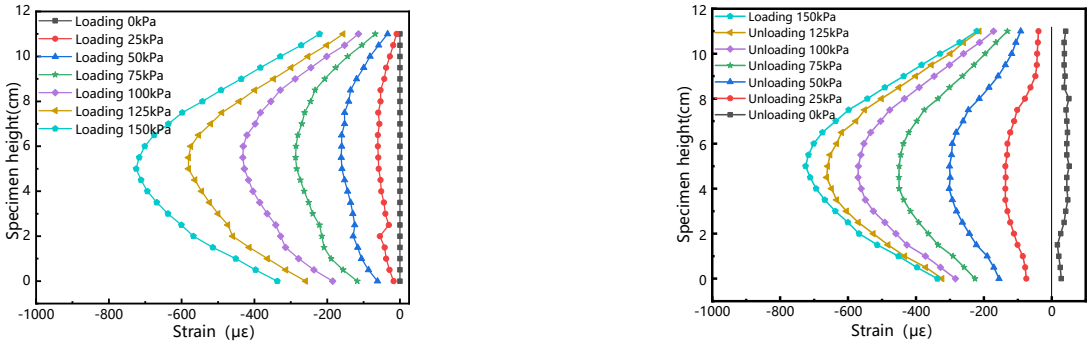

(a) Loading process (b) Unloading process

Fig. 3 Strain distribution of optical fiber under 300 kPa confining pressure

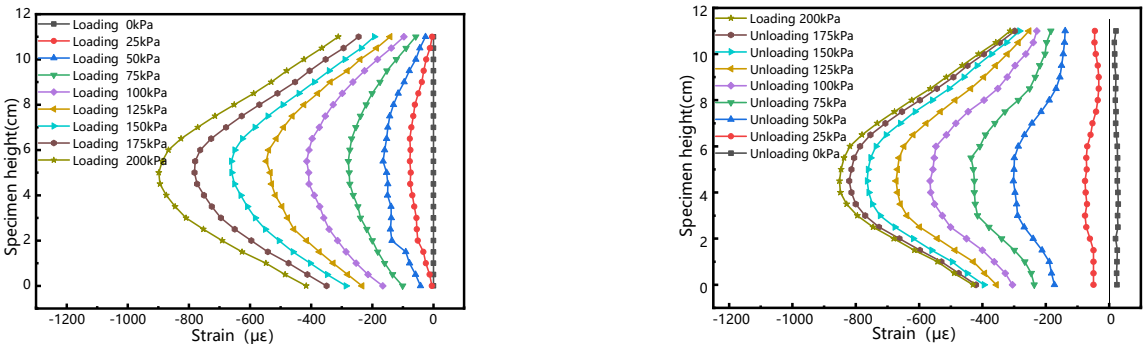

(a) Loading process (b) Unloading process

Fig. 4 Strain distribution of the optical fiber under a 400 kPa confining pressure

under the same axial pressure in the loading process is 384 $\mu\varepsilon$, as shown in Fig. 2(a). When the axial stress was unloaded to 0 kPa, a small tensile fiber strain is observed. The tensile strains under confining pressures of 200, 300, and 400 kPa are approximately 10, 40, and 25 $\mu\varepsilon$, respectively.

3.2 Stress–strain curve

According to the strain distribution of the optical sensing cable along the height of the specimen in Section 3.1, the average strain is calculated according to Eq. (1). The sampling resolution of OFDR in the test is set as d = 5 mm.

$$\varepsilon_f = \frac{\int_0^L \varepsilon(l)dl}{L} = \frac{\sum_1^{\frac{L}{d}} \frac{\varepsilon(i)+\varepsilon(i+1)}{2} d}{L} \tag{1}$$

where ε_f is the average strain of the optical fiber; $\varepsilon(i)$ is the strain of the i-th specimen section; d is the sampling resolution; and L is the specimen height.

Fig. 5 shows the stress–strain curves according to the average strain of the optical sensing cable under different confining pressures. The average strain of the optic cable increases with the axial stress during loading and decreases with the axial stress during unloading. When the axial stress was unloaded to 0 kPa, the average strain of the optical cable shows a small tensile strain.

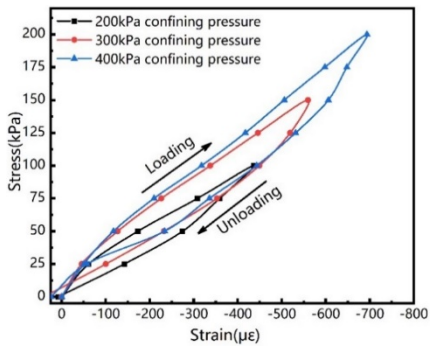

Fig. 5 Stress–strain curves measured by the optical cable under different confining pressures

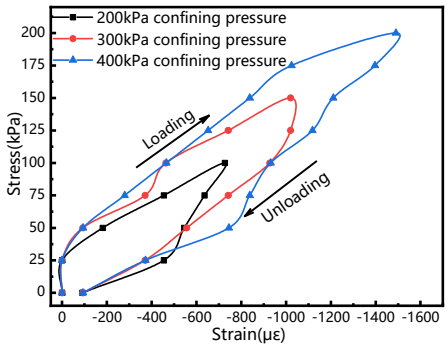

Fig. 6 Stress–strain curves of the specimen under different confining pressures

The average strain of the specimen is calculated by Eq. (2), in which the axial deformation of the specimen was measured by a displacement meter.

$$\varepsilon_m = \frac{\Delta l(i)}{L} \tag{2}$$

where ε_m is the average strain of the specimen, $\Delta l(i)$ is the deformation of the specimen measured by a displacement meter, and L is the length of the specimen.

The hysteresis loop of the specimen is more obvious because of the viscoelasticity of the soil. The hysteresis loop in the stress–strain curves of the sensing cable is the result of the interaction between the sensing cable and the soil, as shown in Fig. 6. The average strain of the specimen is larger than that of the optical sensing cable. However, there is similarity between the average strain and stress of the specimen measured by the displacement meter and the optical sensing cable, which indicates a coordinated deformation relationship between the optical sensing cable and the soil.

Table 3 Linear fitting of cable strain and specimen strain during loading

Confining pressure /kPa	Fitting equation	Correlation coefficient R^2
200	$\varepsilon_f = 0.511\varepsilon_m - 70.68$	0.997
300	$\varepsilon_f = 0.499\varepsilon_m - 66.56$	0.983
400	$\varepsilon_f = 0.531\varepsilon_m - 62.38$	0.998

Table 4 Linear fitting of cable strain and specimen strain during unloading

Confining pressure /kPa	Fitting equation	Correlation coefficient R^2
200	$\varepsilon_f = 0.644\varepsilon_m - 86.03$	0.924
300	$\varepsilon_f = 0.608\varepsilon_m - 106.96$	0.997
400	$\varepsilon_f = 0.567\varepsilon_m - 121.14$	0.973

3.3 Deformation coordination analysis

The strain relationship between the sensing cable and the specimen was analyzed by fitting. As the strain is small at the initial stage of loading and to avoid the relatively large error of the displacement meter for small specimen strain, the strain data for the axial stress from 25 kPa to the maximum stress (100, 150 and 200 kPa) are selected for fitting in the loading process. In the unloading process, the strain data for the axial stress from the secondary unloading stress (75, 125 and 175 kPa) to 0 kPa are selected for fitting.

From Fig. 7, Tables 3 and 4, it can be concluded that there is a good correlation between the average strain of the optical cable and that of the specimen. However, the slopes of the fitting linear equations are different in the loading and unloading process, which indicates a discrepancy in the coordinated deformation performance between the optical

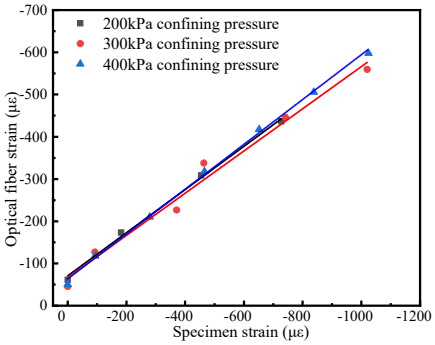

(a) Loading process

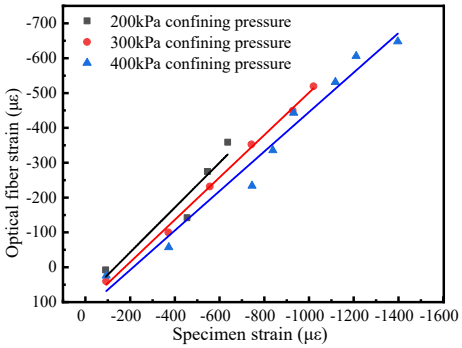

(b) Unloading process

Fig. 7 Relationship between the average strain of the optical cable and that of the specimen

cable and the soil mass. The coordinated deformation performance during unloading is higher than that during loading.

4. Theoretical models

4.1 Strain transfer model

A single mode optical fiber is usually used as a sensor for distributed strain monitoring. The basic structure of a bare optical fiber is a multilayer cylinder composed of a core, cladding and coating. To enhance the mechanical performance and durability of the optical fiber, different types of jackets are added to protect the bare optical fiber, which is called an optical cable. The typical structure of the optical cable is shown in Fig. 8 (Her and Huang 2011, Li *et al*. 2006b).

Fig. 9 shows the boundary condition of the triaxial specimen. A polyurethane sheathed optical sensing cable with a diameter of 2 mm was embedded in the center of the triaxial specimen. A stress-controlled triaxial compression test was applied to produce the axial deformation of the specimen. The axial strain of the specimen was measured by the optical sensing cable and the displacement meter.

Because the sensing cable includes a coating and jacket, there will be a certain loss when the soil strain is transferred to the fiber core. Therefore, to analyze the strain transfer characteristics of the optical sensing cable, a distributed strain transfer model with a coating and jacket is established, as shown in Figs. 10 and 11 (Falcetelli *et al*. 2020, Zhou *et al*. 2007).

The following assumptions are introduced to simplify the analytical strain transfer model:

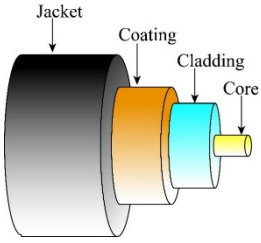

Fig. 8 Typical structure of the optical cable

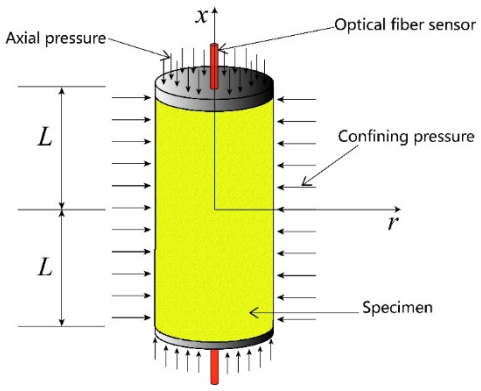

Fig. 9 Stress diagram of the triaxial specimen

(1) The buffer, including the coating and jacket, only bears shear stress. The soil matrix directly bears axial stress and transmits the stress to the optical fiber through shearing between the soil and cable, as well as the buffer, causing the axial deformation of the fiber core;
(2) All interfaces are ideal, and the different layers are well bonded without relative slippage or peeling;
(3) There is no shear stress in the soil except on the surface of the sensing cable;
(4) The optical fiber and buffer are linear elastic materials. Only the elastic–plastic behavior of the soil was considered;
(5) The optical fiber includes a fiber core and cladding, which can be regarded as a whole, commonly known as the fiber core.

Assuming that the length of the optical sensing cable embedded in the soil sample is $2L$, the established coordinate system is shown in Fig. 9. The stress analysis of the model along the X axis is as follows

$$\pi {r_f}^2 d\sigma_f(x) + 2\pi r_f \tau_f(x, r_f)dx = 0 \tag{3}$$

$$2\pi r_f \tau_f(x, r_f)dx = 2\pi r \tau_c(x, r)dx; \qquad r_f \le r \le r_c \tag{4}$$

$$2\pi r_c \tau_c(x, r_c)dx = 2\pi r \tau_j(x, r)dx; \qquad r_c \le r \le r_j \tag{5}$$

$$\pi\left(r^2 - {r_j}^2\right)d\sigma_m(x) + 2\pi r_j \tau_j(x, r_j)dx = 2\pi r \tau_m(x, r)dx; \qquad r_j \le r \le r_m \tag{6}$$

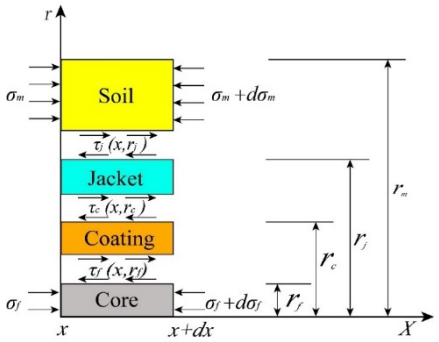

Fig. 10 Stress distribution of the core, coating and jacketing

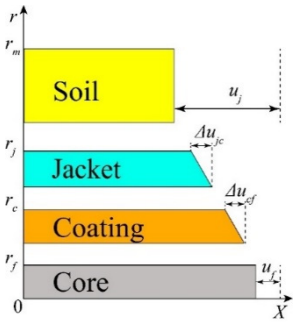

Fig. 11 Displacement distribution of the core, coating and jacketing

where σ is the axial stress, τ is the shear stress, r is the radius from the axis, and subscripts f, c, j, and m represent the fiber core, coating, jacket and soil matrix, respectively.

From Eqs. (3)-(5), we obtain

$$\frac{d\sigma_f(x)}{dx} = -\frac{2\tau_f(x,r_f)}{r_f} \tag{7}$$

$$\tau_c(x,r) = \frac{r_f}{r}\tau_f(x,r_f); \qquad r_f \le r \le r_c \tag{8}$$

$$\tau_j(x,r) = \frac{r_c}{r}\tau_c(x,r_c); \qquad r_c \le r \le r_j \tag{9}$$

Eqs. (7)-(9) are combined to obtain

$$\tau_c(x,r) = -\frac{{r_f}^2}{2r}\frac{d\sigma_f(x)}{dx}; \qquad r_f \le r \le r_c \tag{10}$$

$$\tau_j(x,r) = -\frac{{r_f}^2}{2r}\frac{d\sigma_f(x)}{dx}; \qquad r_c \le r \le r_j \tag{11}$$

The radial displacement of the optical fiber can be ignored because it has a large aspect ratio. Therefore, the following equation can be obtained according to the constitutive equation of the fiber.

$$\tau_c(x,r) = -\frac{{r_f}^2}{2r}\frac{d\sigma_f(x)}{dx} = -\frac{{r_f}^2}{2r}E_f\frac{d\varepsilon_f(x)}{dx}; \quad r_f \le r \le r_c \tag{12}$$

$$\tau_j(x,r) = -\frac{{r_f}^2}{2r}\frac{d\sigma_f(x)}{dx} = -\frac{{r_f}^2}{2r}E_f\frac{d\varepsilon_f(x)}{dx}; \quad r_c \le r \le r_j \tag{13}$$

$$\tau_c(x,r) = G_c\gamma_c(x,r) \cong G_c\frac{du(x,r)}{dr}; \qquad r_f \le r \le r_c \tag{14}$$

$$\tau_j(x,r) = G_j\gamma_j(x,r) \cong G_j\frac{du(x,r)}{dr}; \qquad r_c \le r \le r_j \tag{15}$$

Combining Eqs. (12) and (14), an integral equation is given as follows

$$\int_f^c \left(G_c\frac{du(x,r)}{dr}\right)dr = \int_f^c \left(-\frac{{r_f}^2}{2r}E_f\frac{d\varepsilon_f(x)}{dx}\right)dr \tag{16}$$

$$u(x,r_c) - u(x,r_f) = -\frac{E_f}{G_c}\frac{{r_f}^2}{2}\ln\left(\frac{r_c}{r_f}\right)\frac{d\varepsilon_f(x)}{dx} \tag{17}$$

Substitution of the expression given in Eq. (13) into Eq. (15) gives the integral form as follows

$$\int_c^j \left(G_j\frac{du(x,r)}{dr}\right)dr = \int_c^j \left(-\frac{{r_f}^2}{2r}E_f\frac{d\varepsilon_f(x)}{dx}\right)dr \tag{18}$$

$$u(x,r_j) - u(x,r_c) = -\frac{E_f}{G_j}\frac{{r_f}^2}{2}\ln\left(\frac{r_j}{r_c}\right)\frac{d\varepsilon_f(x)}{dx} \tag{19}$$

Eq. (17) and (19) are combined to obtain

$$u(x,r_j) - u(x,r_f) = -\left[\frac{\ln\left(\frac{r_j}{r_c}\right)}{G_j} + \frac{\ln\left(\frac{r_c}{r_f}\right)}{G_c}\right]E_f\frac{{r_f}^2}{2}\frac{d\varepsilon_f(x)}{dx} \tag{20}$$

The following equations can be obtained by the derivation of Eq. (20)

$$\frac{d^2\varepsilon_f(x)}{dx^2} - k^2\varepsilon_f(x) = -k^2\varepsilon_m(x,r_m) \tag{21}$$

$$k^2 = \frac{2}{[\ln(\frac{r_j}{r_c})/G_j + \ln(\frac{r_c}{r_f})/G_c]E_f{r_f}^2} \tag{22}$$

The soil strain function $\varepsilon_m(x,r_m)$ is necessary for the solution of $\varepsilon_f(x)$ in Eq. (21). The following three cases of the soil strain are discussed.

4.1.1 Uniformly distributed specimen strain

The uniformly distributed specimen strain is as follows

$$\varepsilon_m(x,r_m) = \varepsilon_m \tag{23}$$

According to Ansari and Yuan (1998), we obtain

$$\varepsilon_f(x) = \varepsilon_m\left[1 - \frac{\cosh(kx)}{\cosh(kL)}\right] \tag{24}$$

However, it is different from the previous studies that the strain boundary condition of the sensing cable is not zero in Section 3.1. This is because of the existence of shear stress at the end of the specimen. The strain of the soil can transfer to the fiber core. Here, the strain transfer coefficient at both ends of the specimen can be set as a

$$\varepsilon_f(L) = \varepsilon_f(-L) = a\varepsilon_m \tag{25}$$

Substituting Eq. (25) into Eq. (24) gives

$$\varepsilon_f(x) = \varepsilon_m\left[1 - \frac{(1-a)\cosh(kx)}{\cosh(kL)}\right] \tag{26}$$

The strain transfer coefficient $\alpha(x)$ at each point of the optical cable embedded in the soil is defined as follows

$$\alpha(x) = \frac{\varepsilon_f(x)}{\varepsilon_m} = 1 - \frac{(1-a)\cosh(kx)}{\cosh(kL)} \tag{27}$$

The average strain of the sensing cable is calculated by integrating, and the average strain transfer coefficient can be expressed as follows

$$\bar{\alpha} = \frac{2\int_0^L \varepsilon_f(x)dx}{2L\varepsilon_m} = 1 - \frac{(1-a)\sinh(kL)}{kL\cosh(kL)} \tag{28}$$

After simplification, we obtain

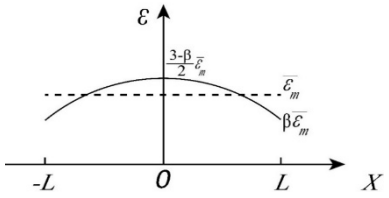

Fig. 12 Parabolic distribution of specimen strain along specimen height

$$\frac{\bar{\alpha}-1}{a-1}=\frac{\sinh(kL)}{kL\cosh(kL)} \tag{29}$$

4.1.2 Parabolic distribution of the specimen strain

During the triaxial compression test, the strain distribution along the height direction of the specimen is not uniform. The distribution of the strain is characterized by a large strain in the middle of the specimen and a small strain at both ends of the specimen, which agrees with the strain distribution measured by the optical sensing cable. Assuming that the strain distribution of the specimen is parabolic, $\varepsilon_m(x,r_m)$ can be expressed as follows

$$\varepsilon_m(x,r_m)=nx^2+b \tag{30}$$

Based on the average strain $\overline{\varepsilon_m}$ measured by the displacement meter and assuming that the strain at both ends of the specimen is $\beta\overline{\varepsilon_m}$ ($0<\beta<1$), the strain distribution of the specimen can be calculated as follows

$$\varepsilon_m(x,r_m)=\frac{3(\beta-1)\overline{\varepsilon_m}}{2L^2}x^2+\frac{3-\beta}{2}\overline{\varepsilon_m} \tag{31}$$

Substituting Eq. (31) into Eq. (21) yields

$$\begin{aligned}&\frac{d^2\varepsilon_f(x)}{dx^2}-k^2\varepsilon_f(x)\\&=-k^2\left[\frac{3(\beta-1)\overline{\varepsilon_m}}{2L^2}x^2+\frac{3-\beta}{2}\overline{\varepsilon_m}\right]\end{aligned} \tag{32}$$

Solving Eq. (32) gives

$$\begin{aligned}\varepsilon_f(x)=&c_1\sinh(kx)+c_2\cosh(kx)\\&+\frac{3(\beta-1)\overline{\varepsilon_m}}{2L^2}x^2+\left[\frac{3-\beta}{2}+\frac{3(\beta-1)}{k^2L^2}\right]\overline{\varepsilon_m}\end{aligned} \tag{33}$$

As the boundary condition of the measured fiber strain is not zero, the strain transfer coefficient of the boundary is also assumed to be a ($0\le a\le 1$). We obtain

$$\varepsilon_f(L)=\varepsilon_f(-L)=a\varepsilon_m(L,r_m)=a\beta\overline{\varepsilon_m} \tag{34}$$

Substituting Eq. (34) into Eq. (33) gives

$$\begin{aligned}\varepsilon_f(x)=&\frac{k^2L^2(a-1)\beta-3(\beta-1)}{k^2L^2\cosh(kL)}\overline{\varepsilon_m}\cdot\cosh(kx)\\&+\frac{3(\beta-1)\overline{\varepsilon_m}}{2L^2}x^2+\left[\frac{3-\beta}{2}+\frac{3(\beta-1)}{k^2L^2}\right]\overline{\varepsilon_m}\end{aligned} \tag{35}$$

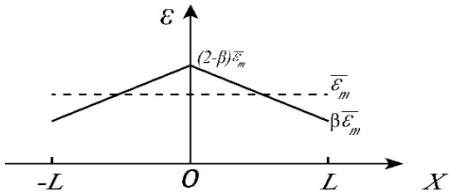

Fig. 13 Symmetrical polyline distribution of specimen strain along specimen height

Similarly, the expression of the strain transfer coefficient α at each point of the optical cable is as follows

$$\alpha(x)=\frac{\frac{k^2L^2(a-1)\beta-3(\beta-1)}{k^2L^2\cosh(kL)}\cdot\cosh(kx)+\frac{3(\beta-1)}{k^2L^2}}{\frac{3(\beta-1)}{2L^2}x^2+\frac{3-\beta}{2}}+1 \tag{36}$$

The average strain of the cable embedded in the specimen is calculated by an integral. The average strain transfer coefficient of the specimen section is obtained as follows

$$\begin{aligned}\bar{\alpha}=&\frac{2\int_0^L\varepsilon_f(x)dx}{2L\overline{\varepsilon_m}}\\=&\frac{[k^2L^2(a-1)\beta-3(\beta-1)]\sinh(kL)}{k^3L^3\cosh(kL)}\\&+\frac{3(\beta-1)}{k^2L^2}+1\end{aligned} \tag{37}$$

4.1.3 Symmetrical polyline distribution of specimen strain

Assuming that the strain distribution of the specimen is a symmetrical polyline during the test, the strain distribution function $\varepsilon_m(x,r_m)$ is expressed as follows

$$\varepsilon_m(x,r_m)=k|x|+b,\qquad -L\le x\le L \tag{38}$$

Similarly, based on the average strain $\overline{\varepsilon_m}$ measured by the displacement meter and assuming that the strain at both ends of the specimen is $\beta\overline{\varepsilon_m}$ ($0<\beta<1$), the strain distribution of the specimen can be calculated as follows

$$\begin{aligned}&\varepsilon_m(x,r_m)=-\frac{(2-2\beta)\overline{\varepsilon_m}}{L}|x|+(2-\beta)\overline{\varepsilon_m},\\&-L\le x\le L\end{aligned} \tag{39}$$

Substituting formulae. (39) into Eq. (21) gives

$$\begin{aligned}\varepsilon_f(x)=&c_1\sinh(kx)+c_2\cosh(kx)\\&-\frac{(2-2\beta)\overline{\varepsilon_m}}{L}|x|+(2-\beta)\overline{\varepsilon_m}\end{aligned} \tag{40}$$

As the boundary condition of the measured fiber strain is not zero, the strain transfer coefficient of the boundary is also assumed to be a ($0\le a\le 1$)

$$\varepsilon_f(L)=\varepsilon_f(-L)=a\varepsilon_m(L,r_m)=a\beta\overline{\varepsilon_m} \tag{41}$$

Substituting Eq. (41) into Eq. (40) gives

$$\varepsilon_f(x) = \frac{(a-1)\beta\overline{\varepsilon_m}}{cosh(kL)}\cosh(kx) - \frac{(2-2\beta)\overline{\varepsilon_m}}{L}|x| + (2-\beta)\overline{\varepsilon_m} \quad (42)$$

Then, the strain transfer coefficients are as follows

$$\alpha(x) = \frac{\varepsilon_f(x)}{\varepsilon_m(x)} = 1 + \frac{\frac{(a-1)\beta\overline{\varepsilon_m}}{cosh(kL)}\cosh(kx)}{-\frac{(2-2\beta)\overline{\varepsilon_m}}{L}|x| + (2-\beta)\overline{\varepsilon_m}} = 1 + \frac{\frac{(a-1)\beta}{cosh(kL)}\cosh(kx)}{-\frac{(2-2\beta)}{L}|x| + (2-\beta)} \quad (43)$$

$$\bar{\alpha} = \frac{2\int_0^L \varepsilon_f(x)dx}{2L\overline{\varepsilon_m}} = 1 + \frac{(a-1)\beta\sinh(kL)}{kLcosh(kL)} \quad (44)$$

4.2 Comparison of the three distribution models

According to Shao *et al*. (2016), it is assumed that the β value is 0.66. The strain distribution of the specimen is obtained by taking β and the strain values of the specimen for various axial pressures into Eqs. (23), (31) and (39) in Section 4.1. The strain transfer coefficient distributions of the above three distribution models are shown in the following figures (*solid line indicates loading*, *dotted line indicates unloading*):

From Figs. 14 to 16, it can be seen that the strain transfer coefficients obtained from different strain distribution models of the specimen have the same characteristics. (1) The strain transfer coefficient is higher in the middle of the specimen and lower at both ends. (2) As the axial pressure increases during loading and decreases during unloading, the strain transfer rate decreases gradually. (3) The strain transfer coefficients are close at each level of axial compression at both ends of the specimens.

In addition, the shapes of the strain transfer coefficient distributions are different. For the symmetrical polyline strain distribution, the strain transfer coefficient in the middle of the specimen is relatively small because the calculated strain value in the middle of the specimen increases sharply.

Ansari and Yuan (1998) indicated that the closer to the middle of the sample, the higher the strain transfer coefficient. According to the experiments of Shao *et al*. (2016), the strain distribution of the triaxial specimen is not uniformly distributed. The strain in the middle of the specimen is larger than that at both ends, which is close to the parabolic type. In summary, it is reasonable to infer that the strain distribution of the specimen is more similar to a parabolic model.

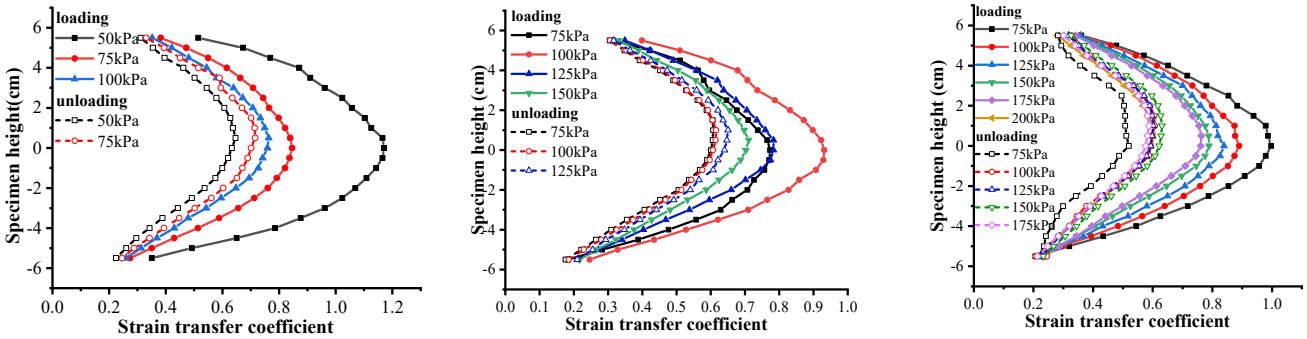

(a) 200 kPa confining pressure (b) 300 kPa confining pressure (c) 400 kPa confining pressure

Fig. 14 Distribution of the strain transfer coefficient under different confining pressures for the uniform strain distribution model

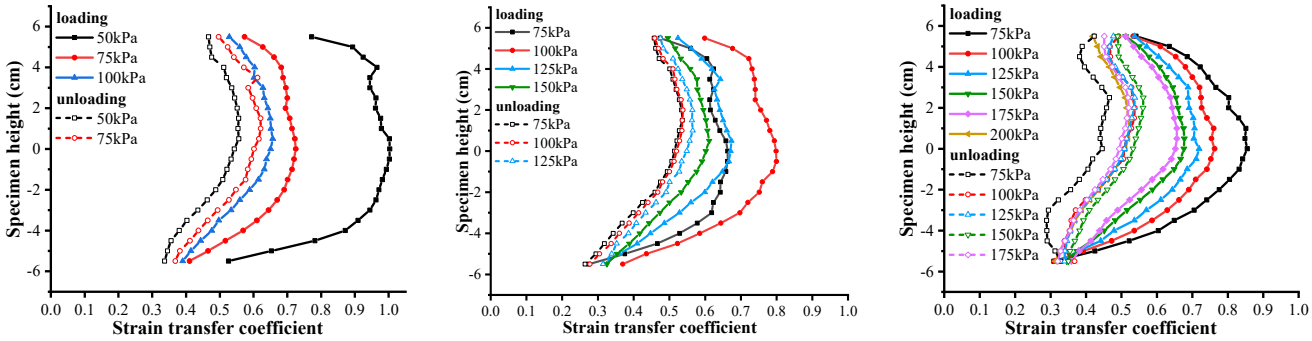

(a) 200 kPa confining pressure (b) 300 kPa confining pressure (c) 400 kPa confining pressure

Fig. 15 Distribution of the strain transfer coefficient under different confining pressures for the parabolic strain distribution model

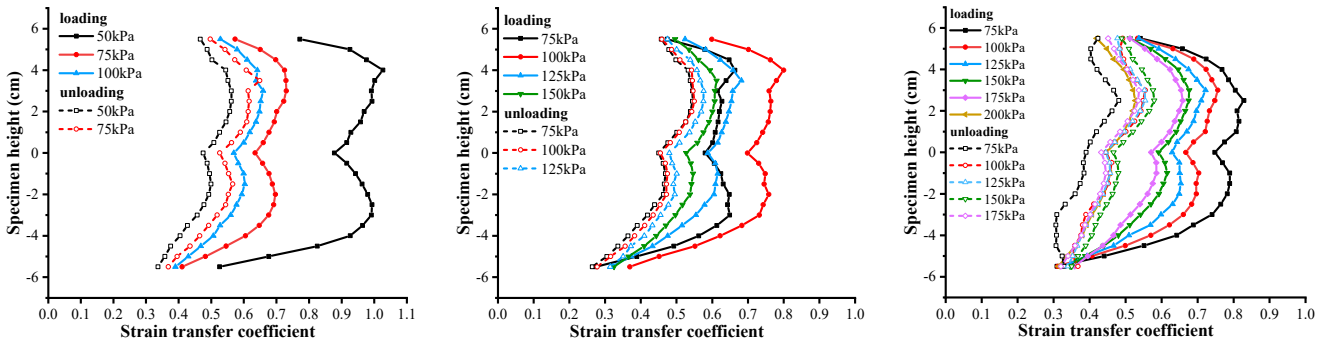

(a) 200 kPa confining pressure (b) 300 kPa confining pressure (c) 400 kPa confining pressure

Fig. 16 Distribution of the strain transfer coefficient under different confining pressures for the symmetrical polyline strain distribution model

Table 5 Parameters of the optical sensing cable

E_f/GPa	r_f/mm	G_c/MPa	r_c/mm	G_j/MPa	r_j/mm
72	0.063	0.27	0.125	80	1

From Figs. 15(a), (b) and (c), it can be seen that the strain transfer rates are different for all axial loadings. However, the strain transfer rates at both ends of the specimen are very close. Therefore, the average value of the strain transfer coefficients at both ends of the specimen under confining pressures of 200, 300 and 400 kPa is calculated as the boundary strain transfer coefficient a, a = 0.425.

Some parameters of the optical sensing cable used in this test are shown in Table 5.

By substituting the parameters in Table 5, the boundary strain transfer coefficients a = 0.425 and β = 0.66 into Eqs. (36) and (37). The average strain transfer rate $\bar{\alpha}$ is 0.788, and the theoretical strain transfer coefficient distribution for the parabolic distribution model of specimen strain is shown in Fig. 17.

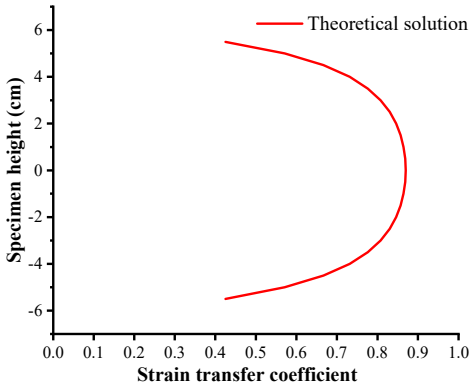

Fig. 17 The theoretical distribution of the strain transfer coefficient for the parabolic distribution model of specimen strain

5. Strain transfer model considering relative slipping of the interfaces

Based on the above analysis, the measured strain transfer coefficient $\bar{\alpha}$ = 0.5 – 0.65 (in Section 3.3) is different from the theoretically calculated strain transfer coefficient $\bar{\alpha}$ = 0.788, especially with increasing axial stress. This is due to the assumption that no relative slippage occurs at the interfaces between the soil, jacket, coating and core. When a sensing cable is embedded in a loose medium, such as loose sand, the shear stress between the optic sensing cable and the soil is likely to exceed its shear strength, which may result in the slipping of the interface.

When the optical cable is embedded in the soil, a relative slippage occurs if the shear stress reaches the peak shear strength between the cable and the soil. The shear stress of the slipping section is equal to the interfacial residual shear strength (Zhang *et al.* 2016). Based on the above analysis, the deformation model shown is proposed in Fig. 18. To simplify the analysis, the cladding and jacket

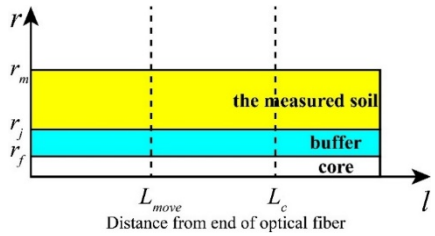

Fig. 18 Deformation model considering interface slipping

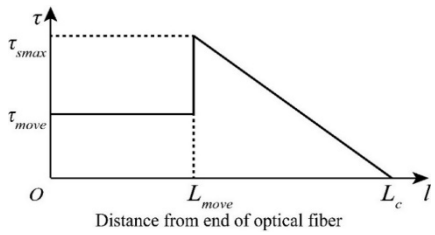

Fig. 19 Assumption of shear stress distribution on the soil-fiber interface

are replaced with a buffer. The shear stress on the interface between the buffer and the measured soil near the end of the optical fiber is assumed, as shown in Fig. 19.

The interfacial shear stress is the residual shear strength at a distance of 0-L_{move} from the end of the optical cable if

relative slippage occurs. Beyond the L_{move} point, there is no relative slippage at the interface, which indicates that the deformation of the optical sensing cable and the soil is the same. The shear stress at the L_{move} point reaches the peak strength. It is assumed that the shear stress decreases linearly with the distance at L_{move}-L_{c}. At the L_{c} point, the shear stress decreases to 0.

According to Fig. 19, the shear stress distribution is as follows

$$\tau(l) = \begin{cases} \tau_{move} & 0 \le l \le L_{move} \\ ml + d & 0 \le l \le L_c \end{cases} \tag{45}$$

where $m = \frac{\tau_{smax}}{L_{move} - L_c}$, $d = \frac{\tau_{smax}}{L_c - L_{move}}$.

According to the static equilibrium conditions of the optical fiber, Eqs. (46) and (47) are obtained

$$\varepsilon_f(l) = \int_0^l \frac{2}{E_f r_f} \tau_{fj}(l) dl \tag{46}$$

$$\varepsilon_f(L_c) = \varepsilon_m \tag{47}$$

For the buffer of the optical cable, according to the equilibrium differential equation of the space axisymmetric problem (Zhang *et al*. 2016), we obtain

$$\frac{\partial \sigma_j(r_j, l)}{\partial l} + \frac{\partial \tau(r, l)}{\partial r} + \frac{\tau_{mj}}{r_j} = 0 \tag{48}$$

Assuming that the shear stress of the buffer is linearly distributed along the radial direction, then

$$\frac{\partial \tau(r, l)}{\partial r} = \frac{\tau_{mj} - \tau_{jf}}{r_j - r_f} \tag{49}$$

By substituting Eqs. (8), (9), (45) and (49) into Eq. (48), we can obtain

$$u_j(r_j, L_{move}) = \frac{1}{E_j}\left(\frac{1}{r_f} - \frac{1}{r_j}\right) \times \left[\frac{m(L_{move}^3 - L_c^3)}{3} + \frac{d(L_{move}^2 - L_c^2)}{2}\right] \tag{50}$$

$$u_m(r_j, L_{move}) = \int_L^{Lmove} \varepsilon_m \, dl = \varepsilon_m(L_{move} - L) \tag{51}$$

In addition, there is no relative slippage at the interface at point L_{move}. Thus

$$u_j(r_j, L_{move}) = u_m(r_j, L_{move}) \tag{52}$$

By substituting Eqs. (45) and (46) into Eq. (47) and then substituting Eqs. (50) and (51) into Eq. (52), the following equations are obtained.

$$\begin{cases} \frac{2r_j\tau_{move}}{r_f^2 E_f} L_{move} + \frac{2r_j}{r_f^2 E_f}[m(L_c^2 - L_{move}^2) - d(L_c - L_{move})] = \varepsilon_m \\ u_j(r_j, L_{move}) = u_m(r_j, L_{move}) \end{cases} \tag{53}$$

The solutions of Eq. (53) are as follows

$$L_{move} = \frac{r_f^2 E_f \varepsilon_m}{2r_j(\tau_{smax} - \tau_{move})} \tag{54}$$

$$L_c = \frac{\sqrt{25L_{move}^2 - \frac{72\varepsilon_m(L_{move} - L)}{B\tau_{smax}}} - L_{move}}{6} \tag{55}$$

where $B = \frac{1}{E_j}\left(\frac{1}{r_f} - \frac{1}{r_j}\right)$.

The values of L_{move} and L_c can be calculated by substituting the cable parameters into Eqs. (54) and (55). The slip length of the soil-cable interface, optical fiber strain distribution and strain transfer coefficient can be obtained when the end interface slippage is considered.

To obtain the shear strength of the interface between the optical cable and soil, a series of pull-out tests were carried out. The typical values of peak strength τ_{smax} and residual strength of the interface τ_{move}. are 80 kPa and 70 kPa, respectively.

Substituting the parameters of the optical cable in Table 5 into Eqs. (54) and (55), we obtain

$$L_{move} = 0.0562\ m \tag{56}$$

$$L_c = 0.0372\ m \tag{57}$$

Therefore, there is a relative slippage between the optical cable and the soil within 0.0562 m from the end. It can be inferred that there is a relative slip for the full length of the triaxial specimen because the half length of the specimen is only 0.055 m. The interface slippage between the soil and the cable has a significant impact on the strain measurement accuracy of the optical sensing cable.

6. Conclusions

In this paper, the instrument is refitted into the distributed optical fiber sensor module based on ground settlement monitoring, and optical frequency domain reflection (OFDR) technology is used to measure the optical fiber-soil coordinated deformation test. Triaxial testing was adopted to simulate the compression deformation of the soil at different depths. The strain distribution of the optical sensing cable and the axial deformation of the soil specimen were measured and compared. Theoretical strain transfer models were proposed to analyze the performance of deformation coordination between the sensing cable and the soil. The main conclusions are as follows:

(1) Although the cable strain measured by OFDR is different from the specimen strain measured by the displacement meter, they have a good linear relationship. It can be inferred that the distributed

optical fiber sensor is feasible for the deformation monitoring of soil given that the strain transfer coefficient between the sensing cable and the soil is obtained.

(2) A more reasonable strain transfer model between the optical sensing cable and the soil was established based on the measured strain transfer coefficient with the consideration of three different strain distributions of the triaxial specimen. The parabolic stain distribution model has a higher strain transfer performance than the uniformly distributed strain model and the symmetrical polyline strain model. It can be deduced that the strain transfer coefficient is affected by interface slippage

(3) The proposed triaxial testing method can be adopted to evaluate the performance of the deformation coordination between the optical sensing cable and the soil. The strain transfer coefficient can be used in monitoring applications of soil compression, such as ground subsidence, to modify the measured strain.

Acknowledgments

The authors acknowledge the support of the National Natural Science Foundation of China (No. 42077233) and the Open Project of Key Laboratory of Earth Fissures Geological Disaster of the Ministry of Land and Resources (No. JSDDY-HJ-D-2018-021).

References

Al-Tarawneh, M., Huang, Y., Lu, P. and Tolliver, D. (2018), "Vehicle classification system using in-pavement fiber Bragg grating sensors", *IEEE Sensors J.*, **18**(7), 2807-2815. https://doi.org/10.1109/JSEN.2018.2803618

Ansari, F. (2007), "Practical implementation of optical fiber sensors in civil structural health monitoring", *J. Intell. Mater. Syst. Struct.*, **18**(8), 879-889. https://doi.org/10.1177/1045389X06075760

Ansari, F. and Yuan, L.B. (1998), "Mechanics of bond and interface shear transfer in optical fiber sensors", *J. Eng. Mech.-ASCE*, **124**(4), 385-394. https://doi.org/10.1061/(ASCE)0733-9399(1998)124:4(385).

Billon, A., Jean-Marie, H., Quiertant, M., Taillade, F., Khadour, A., Martin, R.-P. and Benzarti, K. (2015), "Qualification of a distributed optical fiber sensor bonded to the surface of a concrete structure: A methodology to obtain quantitative strain measurements", *Smart Mater. Struct.*, **24**(11), 115001. https://doi.org/10.1088/0964-1726/24/11/115001.

Claus, R.O., Bennett, K.D., Vengsarkar, A.M. and Murphy, K.A. (1989), "Embedded optical fiber sensors for materials evaluation", *J. Nondestr. Eval.*, **8**(2), 135-145. https://doi.org/10.1007/BF00565637

Falcetelli, F., Rossi, L., Sante, R. and Bolognini, G. (2020), "Strain Transfer in Surface-Bonded Optical Fiber Sensors", *Sensors*, **20**(11), 3100. https://doi.org/10.3390/s20113100

Feng, X., Wu, W., Li, X., Zhang, X. and Zhou, J. (2015), "Experimental investigations on detecting lateral buckling for subsea pipelines with distributed fiber optic sensors", *Smart Struct. Syst., Int. J.*, **15**(2), 245-258. https://doi.org/10.12989/SSS.2015.15.2.245

Glisic, B. and Yao, Y. (2012), "Fiber optic method for health assessment of pipelines subjected to earthquake-induced ground movement", *Struct. Health Monitor.*, **11**(6), 696-711. https://doi.org/10.1177/1475921712455683

Gutiérrez, F., Galve, J.P., Lucha, P., Castañeda, C., Bonachea, J. and Guerrero, J. (2011), "Integrating geomorphological mapping, trenching, InSAR and GPR for the identification and characterization of sinkholes: A review and application in the mantled evaporite karst of the Ebro Valley (NE Spain)", *Geomorphology*, **134**(1-2), 144-156. https://doi.org/10.1016/j.geomorph.2011.01.018

Habel, W.R. and Krebber, K. (2011), "Fiber-optic sensor applications in civil and geotechnical engineering", *Photonic Sensors*, **1**(3), 268-280. https://doi.org/10.1007/s13320-011-0011-x

Her, S.C. and Huang, C.Y. (2011), "Effect of Coating on the Strain Transfer of Optical Fiber Sensors", *Sensors*, **11**(7), 6926-6941. https://doi.org/10.3390/s110706926

Hu, R.L., Yue, Z.Q., Wang, L.C. and Wang, S.J. (2004), "Review on current status and challenging issues of land subsidence in China", *Eng. Geol.*, **76**(1), 65-77. https://doi.org/10.1016/j.enggeo.2004.06.006

Huang, Y., Lu, P. and Tolliver, D. (2018), "Vehicle classification system using in-pavement fiber Bragg grating sensors", *IEEE Sensors J.*, **18**(7), 2807-2815. https://doi.org/10.1109/JSEN.2018.2803618

Iten, M. (2011), "Novel Applications of Distributed Fiber-optic Sensing in Geotechnical Engineering", Ph.D. Dissertation; ETH, Switzerland.

Kesavan, K., Ravisankar, K., Parivallal, S. and Sreeshylam, P. (2005), "Applications of fiber optic sensors for structural health monitoring", *Smart Struct. Syst., Int. J.*, **1**(4), 355-368. https://doi.org/10.12989/sss.2005.1.4.355

Klar, A., Dromy, I. and Linker, R. (2014), "Monitoring tunneling induced ground displacements using distributed fiber-optic sensing", *Tunnell. Undergr. Space Technol.*, **40**, 141-150. https://doi.org/10.1016/j.tust.2013.09.011

Leung, C.K.Y., Wan, K.T., Inaudi, D., Bao, X., Habel, W., Zhou, Z., Ou, J., Ghandehari, M., Wu, H.C. and Imai, M. (2015), "Review: optical fiber sensors for civil engineering applications", *Mater. Struct.*, **48**(4), 871-906. https://doi.org/10.1617/s11527-013-0201-7

Li, C., Tang, X. and Ma, T. (2006a), "Land subsidence caused by groundwater exploitation in the Hangzhou-Jiaxing-Huzhou Plain, China", *Hydrogeol. J*, **14**(8), 1652. https://doi.org/10.1007/s10040-006-0092-6

Li, D.S., Li, H.N., Ren, L. and Song, G. (2006b), "Strain transferring analysis of fiber Bragg grating sensors", *Optical Eng.*, **45**(2), 024402. https://doi.org/10.1117/1.2173659

Morton, R.A. and Bernier, J.C. (2010), "Recent Subsidence-Rate Reductions in the Mississippi Delta and Their Geological Implications", *J. Coastal Res.*, **26**(3), 555-561. https://doi.org/10.2112/JCOASTRES-D-09-00014R1.1

Nanni, A., Yang, C.C., Pan, K., Wang, J.S. and Jr, R. (1991), "Fiber-optic sensors for concrete strain-stress measurement", *ACI Mater. J.*, **88**(3), 257-264. https://doi.org/10.14359/1785

O'Leary, M. and Gottardi, R. (2020), "Relationship between Growth Faults, Subsidence, and Land Loss: An Example from Cameron Parish, Southwestern Louisiana, USA", *J. Coastal Res.*, **36**(4), 812-827. https://doi.org/10.2112/Jcoastres-D-19-00108.1

Shao, L.T., Liu G.T., Zeng F.T. and Guo X.S. (2016), "Recognition of the Stress-Strain Curve Based on the Local Deformation Measurement of Soil Specimens in the Triaxial Test", *Geotech. Test. J.*, **39**, 20140273. https://doi.org/10.1520/GTJ20140273

Tennyson, R., Mufti, A., Rizkalla, S., Tadros, G. and Benmokrane, B. (2001), "Structural Health Monitoring of innovative bridges in Canada with fiber optic sensors", *Smart Mater. Struct.*, **10**(3), 560. https://doi.org/10.1088/0964-1726/10/3/320

Wan, K.T., Leung, C.K.Y. and Olson, N.G. (2008), "Investigation of the strain transfer for surface-attached optical fiber strain sensors", *Smart Mater. Struct.*, **17**(3), 035037. https://doi.org/10.1088/0964-1726/17/3/035037

Wang, H. and Zhou, Z. (2014), "Advances of strain transfer analysis of optical fibre sensors", *Pacific Sci. Rev.*, **16**(1), 8-18. https://doi.org/10.1016/j.pscr.2014.08.002

Wang, G.Y., You, G., Shi, B., Yu, J. and Tuck, M. (2009), "Long-term land subsidence and strata compression in Changzhou, China", *Eng. Geol.*, **104**(1), 109-118. https://doi.org/10.1016/j.enggeo.2008.09.001

Yao, G. and Mu, J. (2008), "D-InSAR Technique for Land Subsidence Monitoring", *Earth Sci. Front.*, **15**(4), 239-243. https://doi.org/10.1016/S1872-5791(08)60059-7

Zhang, C.C., Zhu, H.H., Shi, B., She, J.K. and Zhang, D. (2016), "Performance evaluation of soil-embedded plastic optical fiber sensors for geotechnical monitoring", *Smart Struct. Syst., Int. J.*, **17**(2), 297-311. https://doi.org/10.12989/SSS.2016.17.2.297

Zhang, D., Wang, H., Xu, Q., Zheng, G. and Bezuijen, A. (2017), "Internal deformation monitoring for centrifuge slope model with embedded FBG arrays", *Landslides*, **14**(1), 407-417. https://doi.org/10.1007/s10346-016-0742-2

Zhang, D.Q., He, J., Xue, Y., Xu, J. and Xu, X. (2019), "Investigation of settlement monitoring method based on distributed Brillouin fiber optical sensor", *Measurement*, **134**, 118-122. https://doi.org/10.1016/j.measurement.2018.10.081

Zhou, Z., Li, J. and Ou, J. (2007), "Interface transferring mechanism and error modification of embedded FBG strain sensors", *Front. Electr. Electron. Eng. China*, **2**(1), 92-98. https://doi.org/10.1007/s11460-007-0017-8

CC